International Journal of Hydrogen Energy 61 (2024) 162–172

Contents lists available at ScienceDirect

International Journal of Hydrogen Energy

journal homepage: www.elsevier.com/locate/he

Impact of Co:Fe cations composition in amorphous and mesoporous cobalt iron phosphate electrocatalysts synthesized by SILAR method on durable electrochemical water splitting

Suraj A. Khalate [a], Sujit A. Kadam [b], Yuan-Ron Ma [b], Sambhaji S. Kumbhar [a], Shraddha B. Bhosale [a], Vinod V. Patil [a], Vinayak G. Parale [d], Sachin B. Kulkarni [c], Chandrakant D. Lokhande [a], Hyung-Ho Park [d,**], Umakant M. Patil [a,d,*]

[a] Centre for Interdisciplinary Research (CIR), D. Y. Patil Education Society, Kolhapur, 416 006, India
[b] Department of Physics, National Dong Hwa University, Hualien, 97401, Taiwan
[c] Department of Physics, Tuljaram Chaturchand College, Baramati, 413 102, India
[d] Department of Materials Science and Engineering, Yonsei University, 50 Yonsei-ro, Seodaemun-gu, Seoul, 03722, South Korea

ARTICLE INFO

Handling Editor: Dr J Ortiz

Keywords:
Amorphous thin film electrocatalyst
Cations composition variation
SILAR method
Electrochemical water splitting

ABSTRACT

Efficient and durable electrocatalysts are crucial for energy conversion devices that perform the oxygen evolution reaction (OER) and hydrogen evolution reaction (HER). The structural and morphological characteristics of the electrocatalyst can significantly impact the HER/OER performance. Therefore, it is essential to develop a high-performing electrocatalyst with desired properties using a simple and cost-effective chemical process. So, herein, successive ionic layer adsorption and reaction (SILAR) deposited amorphous, hydrous cobalt iron phosphate (CFP) thin film electrocatalysts are implemented toward electrochemical water splitting. Moreover, in the present work, the molar proportions of cobalt and iron were streamlined to study their synergistic effect on electrochemical HER and OER performance. The electrode of best-performing (CFP–S2) requires the lowest overpotentials of 242 mV for OER and 67.9 mV for HER at a current density of 10 mA/cm^2, which maintains its activity after 24 h. The alkaline water splitting into a similar electrolytic bath using two electrode systems was demonstrated for 100 h with the lowest overpotential of 1.72 V. The remarkable electrochemical performance and postmortem analysis unambiguously demonstrate that CFP electrodes are a highly promising and robust option for long-duration water-splitting devices, and the facile SILAR method for scalable CFP electrode synthesis indicates enormous potential for commercial applications.

1. Introduction

Hydrogen is a prospective energy source that is profitable to grab the market in the renewable energy sector [1,2]. A primary source of renewable energy has been suggested: hydrogen and has been termed 'transitioning to a hydrogen society' [3–5]. Various methods are used to produce hydrogen from different sources, such as reforming steam of natural gas, coal gasification, oxidation of methane, carbon/-hydrocarbon assisted water electrolysis, radiolysis, thermolysis, photo-catalytic water splitting, fermentative hydrogen production, photobiological water splitting, biocatalysts electrolysis, enzymatic hydrogen generation, etc. [6–8]. Among them, the most practical and cost-efficient method of producing water splitting is electrochemical for generating oxygen and hydrogen [1,2]. Two half-reactions, specifically the hydrogen evolution reaction (HER) and the oxygen evolution reaction (OER), form the electrochemical process of splitting water, and it requires 1.23 V a theoretical potential to initiate water splitting [9,10]. To split water, excess energy or overpotential is necessary to overcome the barrier of activation energy caused by kinetic effects. Therefore, researchers have been making significant efforts to develop excellent catalysts to decrease the overpotential of water splitting. However, thermodynamics does not favor the direct dissociation of water into hydrogen and oxygen under normal pressure and temperature. Even though the HER process is much more promising in an acidic electrolytic

* Corresponding author. Centre for Interdisciplinary Research (CIR), D. Y. Patil Education Society, Kolhapur, 416 006, India.
** Corresponding author. Department of Materials Science and Engineering, Yonsei University, 50 Yonsei-ro, Seodaemun-gu, Seoul, 03722, South Korea.
E-mail addresses: hhpark@yonsei.ac.kr (H.-H. Park), umakant.physics84@gmail.com (U.M. Patil).

https://doi.org/10.1016/j.ijhydene.2024.02.259
Received 23 September 2023; Received in revised form 24 January 2024; Accepted 19 February 2024
Available online 1 March 2024
0360-3199/© 2024 Hydrogen Energy Publications LLC. Published by Elsevier Ltd. All rights reserved.

environment, the overall splitting of water depending on non-noble metal catalysts is generally worked out using an alkaline solution medium.

Electrocatalysts play a significant role in facilitating this reaction by increasing the kinetics of electron transfer. The potential essential to accelerate the reaction above the 1.23 V threshold, which is typically in a region of 0.3–0.5 V vs the reversible hydrogen electrode (RHE), is known as the overpotential for the process of oxygen evolution. In contrast, the overpotential required to drive the HER is essentially 0 V vs RHE at a platinum (Pt) electrode interface. To reduce overpotential and reduce energy loss throughout the OER, an appropriate electrocatalyst must have exceptional catalytic performance, enhanced electrical conductivity, easy transfer of mass and gas dissipation, and sufficient electrocatalytic durability [11]. However, Pt being an expensive material gives rise to the question of cost-effectiveness. Noble metal-based expensive catalyst materials such as state-of-the-art like Pt, ruthenium (Ru), and iridium oxide (IrO_2) are stamped as top catalysts in OER because of their low overpotential, good current density, low Tafel slope, etc. [12–14]. Nevertheless, noble metals have very rare resources available in the earth's crust and hence are very expensive; also, these catalysts have poor OER performance at higher current densities in the alkaline medium than transition metal-based catalysts [15–18]. To date, various transition metals (TMs) and their compounds, including hydroxides, oxides, selenides, sulphides, nitrides, borides, phosphides, and carbides exhibit diverse performances for electrochemical water splitting [19,20]. However, they suffer from poor electrochemical results due to poor electrical conductivity and high electrical resistance and hence slow ion transfer rate. So, it is imperative to prioritize the development of inexpensive, readily available, and exceptionally performing materials for electrochemical water splitting. Therefore, a variety of strategies were employed by various research groups to enhance the electrochemical catalytic property through structural modifications, such as proper surface topography, large surface area, and high surface activity [21–23].

TM phosphate (TMPs) based electrocatalysts show favorable performance for electrocatalytic water splitting, providing alleviated active sites and adsorption. Proton-coupled electron transfer is another way that phosphate ions or molecules aid in the oxidation of metal atoms while disturbing native atomic configuration, which is advantageous for the adsorption and oxidation of electrolyte ions. Among TMPs, cobalt iron phosphate (CFP) is the most intriguing material for oxidation of water. CFP has been synthesized by various methods such as hydrothermal [24], coprecipitation [25,26], solvothermal [27], microwave heating [28], and solution plasma method [29]. To permit access to active sites, effective mass transfer, and the release of gases, the optimal catalyst for water splitting requires a spacious, porous structure, a significant area of surface, and a tailored reaction interface. Structural disorder and intrinsic defect formation are beneficial to the electrochemical process because arbitrarily situated bonds are common in amorphous materials, especially those connected to unsaturated electronic configurations, which are characterized by structural and chemical deviations. The adsorption of electrolytic ions and the electron transfer that results in the formation of intermediate states take place at these randomly positioned bonds with deficient electronic configurations. A long-range crystalline structure can have difficulty in deforming during the catalytic process, limiting the percolation of ions throughout the material layer. In contrast, short grain boundaries and a large number of defects in short-range ordered crystalline or amorphous materials provide easy ion diffusion leading to better performance [30,31]. SILAR is one of the best method for the preparation of amorphous materials at a large scale and is the simplest, economically cheap, versatile, and environmentally friendly known soft chemical solution method to deposit thin films in ambient conditions [32]. However, there are currently no reports on the use of CFP thin films prepared by the SILAR method for electrochemical water splitting.

In the present work, we have prepared binder-free CFP electrocatalyst electrodes on stainless-steel (SS) substrate using the SILAR method, where SS substrates are the ideal choice because of their good electrical low-cost, conductivity, and non-reactivity in both acidic and alkaline environments, compared to Ni foam. The thin films of CFP were synthesized by changing the concentration ratio between cobalt and iron while maintaining the phosphorous and oxygen at constant proportion to investigate synergy among the cations (Co:Fe). The effect of chemical compositional (Co:Fe) variation on the structure, surface electronic states, morphology, stoichiometry, and electrocatalytic OER, HER, and overall water splitting was analyzed. Furthermore, material robustness was studied for optimized catalyst electrodes in the alkaline medium for at least 100 h by constructing a two-electrode overall water splitting system and demonstrated herein.

2. Experimental section

2.1. Materials and substrates cleaning procedure

The chemicals (analytical grade) were used for the synthesis of CFP such as $CoCl_2{\cdot}6H_2O$, $FeCl_2$, and K_2HPO_4 bought from Sigma-Aldrich. The synthesis of CFP was carried out by using purchased chemicals without any changes in it. SS substrates were properly cleaned before the reaction's preliminary steps. The pieces of SS substrates (1×5 cm^2) were polished using polish paper (zero grade), proceeded by numerous rinses using double distilled water (DDW), and soap solution. Following this, the substrates underwent a 20 min ultrasonic cleaning procedure using a solution comprising ethanol and DDW before being employed in the subsequent deposition process.

2.2. Cobalt iron phosphate thin films synthesis

The thin films of CFP were prepared at ambient temperature by the low-cost and facile SILAR method. The solutions were prepared individually in 50 ml DDW by dissolving 0.125 M K_2HPO_4 in a beaker served as anionic precursor and another beaker was prepared containing the different concentrations of $CoCl_2{\cdot}6H_2O$ (0.08 M–0.00 M) and $FeCl_2$ (0.00 M–0.08 M) which served as cationic precursor. The detailed reaction parameters are described in Table S1. In between each precursor, beakers of 50 ml DDW were arranged for the rinsing purpose. That means, there were four beakers arranged in sequence as cationic precursor (Co^{2+} and Fe^{2+}), DDW, anionic precursor (PO_4^{3-}), and DDW as shown in Fig. 1. The well-cleaned SS substrates were immersed in each beaker successively. This procedure completes the one cycle of the deposition. The adsorption time (20 s), first rinsing time (10 s), reaction time (20 s), and second rinsing time (10 s) were optimized with the 50 cycles to get a well-adherent and uniform film. After completion of reaction cycles, faint violet to faint yellow-colored thin films were obtained. The developed thin films of CFP were designated as CFP series (CFP-S1-CFP-S5).

2.3. Physico-chemical characterizations

The X-ray diffraction (XRD) data of the CFP films were obtained by the X-ray diffractometer 'Rigaku Miniflex 600' with Cu–K target radiation ($\lambda = 1.5406$ Å). Fourier transform infrared spectroscopy (FT-IR) study carried out on the spectroscope of ALPHA (II) Bruker in the region of 400–4000/cm was used to analyze molecular vibrations. Belsorp II mini was employed to evaluate pore size distribution and surface area using isotherms of N_2 adsorption-desorption. Field emission-scanning electron microscope (FE-SEM, JEOL JSM-6500F) was utilized to examine the compositional and surface morphological properties. Transmission electron microscopy (TEM) analysis using a JEM-2100F JEOL instrument was conducted at an acceleration voltage of 125 kV to investigate morphology and elemental analysis of the material. Using microfocus monochromatic Al K X-ray light from Thermo Scientific Inc.'s K-alpha instrument, electronic state information was determined

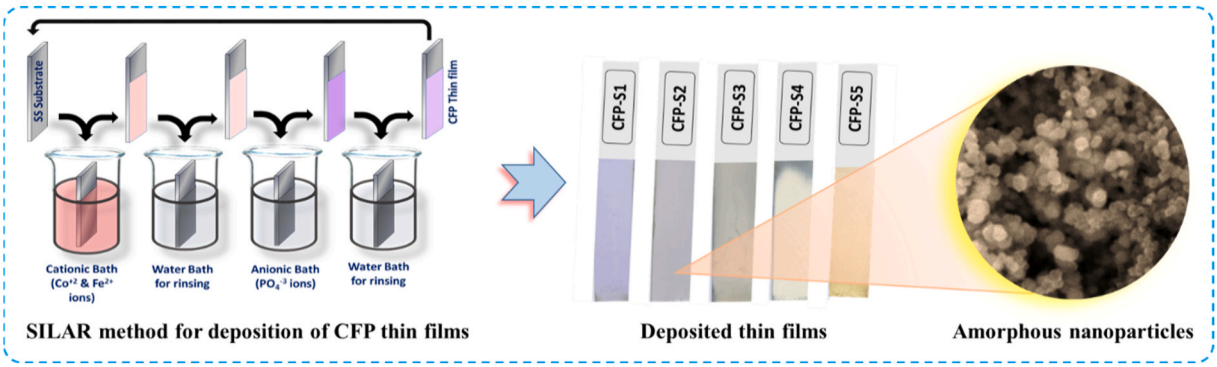

Fig. 1. Schematic representation of SILAR method employed to deposit amorphous nanoparticles CFP in thin film form.

using X-ray photoelectron spectroscopy (XPS).

2.4. Electrochemical characterizations

The electrochemical study of the CFP electrocatalyst was measured on the PARSTAT 3000A-DX electrochemical workstation (AMETEK Scientific Instruments USA) using a standard three-electrode electrochemical cell setup. The working electrode was made of SS metal plates deposited with CFP thin films, having a predetermined 1 cm^2 surface area. The reference electrode is used as a saturated calomel electrode (SCE) submerged in a saturated KCl solution. The OER study was performed in a 1 M KOH electrolyte solution with a pH of 13.7, while the HER was performed in a 1 M H_3PO_4 electrolyte solution with a pH of 1.5. The equation: $V_{RHE} = V_{SCE} + 0.059 \times pH + 0.241$ was utilized to convert voltage from SCE to RHE. At varied scan rates, cyclic voltammetry (CV) curves were acquired to determine the electrochemically active surface area (ECSA) in the potential window of 1.05–1.2 V versus RHE. The curves of polarization were collected using linear sweep voltammetry (LSV) at a scan rate of 1 mV/s in the potential range 1.05–1.75 V vs RHE (for OER) and 0.33 to −0.65 V vs RHE (for HER) to assess the response of electrochemical catalytic. Electrochemical impedance spectroscopy (EIS) was investigated at open circuit potential (OCP) with a 10 mV amplitude in a frequency region of 0.1 MHz–100 mHz. Chronoamperometry (CA) measurements at overpotentials were used to conduct studies on long-term catalytic stability. Furthermore, overpotentials (V) were determined by subtracting the measured potential (RHE) from the thermodynamic potential values of 1.23 V for OER and 0 V for HER. A full-cell electrolyzer was constructed using a two-electrode system, with deposited CFP electrodes serving as both cathode and anode, and electrochemically characterized in the same alkaline electrolyte for water splitting and durability testing.

3. Results and discussion

3.1. Reaction mechanism

The SILAR method is a material synthesis process that involves ion-by-ion nucleation, solid phase development, coalescence, and layer-by-layer film formation from the reaction solution. Upon immersion of the substrate in Co^{2+} and Fe^{2+} cationic precursor solution, the metal ions get attracted towards the substrate by the cohesive or van der Waals force, and the Helmholtz electric double layer is formed due to the adsorption of Co^{2+} and Fe^{2+} cations present in the precursor solution [33].

$$CoCl_2.6H_2O + FeCl_2 + nH_2O \rightarrow Co^{2+} + Fe^{2+} + 4Cl^- + (n+6)H_2O \quad (1)$$

The loosely bound ions were rinsed out by dipping the substrate in the next beaker of DDW. For the reaction with anions, the substrates were vertically immersed in the beaker containing a solution of anionic precursor. As the anionic precursor is K_2HPO_4, it becomes:

$$K_2HPO_4 + nH_2O \rightarrow HPO_4^{2-} + 2K^+ + nH_2O \quad (2)$$

Here, the adsorbed Co^{2+} and Fe^{2+} cations react with the PO_4^{3-} anions and neutralize making the solid substance on the surface of the substrate.

$$xCo^{2+} + (3-x)Fe^{2+} + 2HPO_4^{2-} \rightarrow Co_xFe_{3-x}(PO_4)_2 + 2H^+ \quad (3)$$

Loosely bounded solid particles were rinsed by immersing the substrate in the next beaker of DDW. The development of CFP ($Co_xFe_{3-x}(PO_4)_2$) at the ionic stage occurred by following heterogenetic nucleation on the substrate surface of SS. These nuclides propagate layer-by-layer to prepare a thin coating of CFP. The synthesis method and deposited thin films are represented schematically in Fig. 1 and the mass loading for each sample calculated by weight difference method is shown in Fig. S1. The uniform growth rate of the CFP thin film electrodes is evident from the negligible variation in the mass of each electrode, also attributed to the quite similar mass of Co/Fe. The obtained CFP series electrocatalysts were used for OER and HER, and the best-performed electrode was used for overall water splitting in alkaline electrolytes.

3.2. Structural, morphological, and compositional analysis

To study the structural characteristics of SILAR-deposited CFP-S1, CFP-S2, CFP-S3, CFP-S4, and CFP-S5 materials on SS substrates, XRD patterns were recorded as displayed in Fig. 2(A). The XRD patterns of CFP series samples show the amorphous nature and the diffraction peaks denoted with '*' are for the SS substrate. It is difficult for a firmly crystalline structure to stretch or contract, which in turn limits ion penetration and diffusion. On the other hand, amorphous materials undergo a continuous redox reaction that permeates their bulk and extends beyond their surface. Compared to crystalline formations, this leads to better performance [31]. Generally, amorphous electrocatalysts offer several advantages over their crystalline counterparts. Firstly, they have abundant dangling bonds or coordinately unsaturated atoms, providing more active sites to promote electrochemical catalytic performance. Secondly, the intrinsic structural disorder and rich defects are helpful in facilitating ion diffusion and charge transfer through amorphous materials. Lastly, flexible and metastable structures allow adaptive self-reconstruction, facilitating reaction kinetics and exceptional stability [34,35].

By using the FT-IR spectroscopy, CFP series samples were characterized to study the molecular bonding as shown in Fig. 2(B), from wavenumber 400 to 4000/cm containing intermolecular vibrational modes of phosphate anions (PO_4^{3-}) and structural water molecules. The PO_4 bond's asymmetric bending vibrational mode is indicated by the presence of a peak of absorption at 595 cm^{-1}. A small absorption at 773/cm corresponds to surface adsorbed =C–H from the environment. The sharp absorption at 1035/cm shows the asymmetric stretching

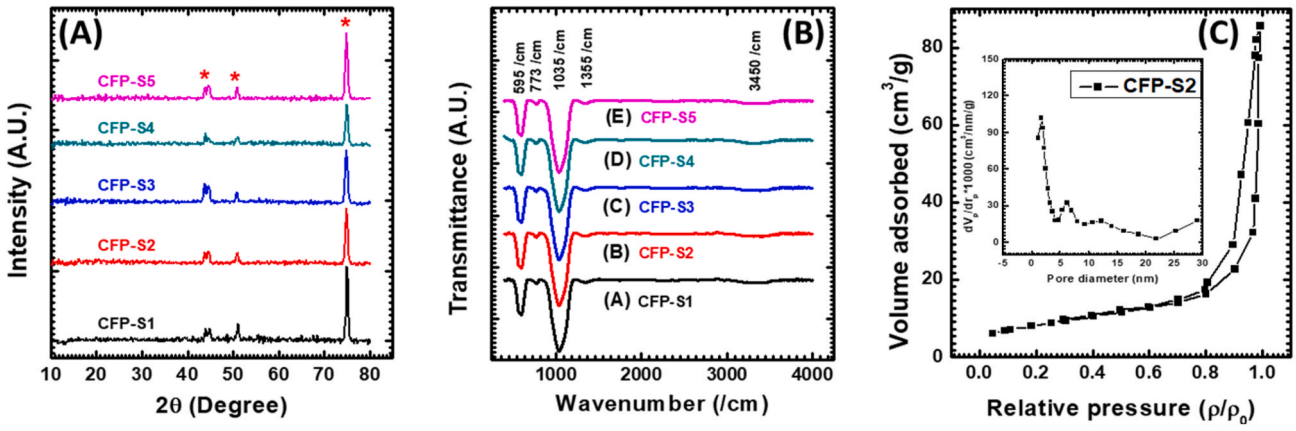

Fig. 2. **(A)** XRD, **(B)** FT-IR analysis of CFP thin film materials, and **(C)** N_2 sorption curves (inset: pore size distribution) of CFP-S2 thin film electrocatalyst.

vibrations of PO_4 [36]. The surface-adsorbed CO_2 molecules are shown by a small absorption band at 1355/cm [37]. The large bands of absorption in the region of wavenumber 3000–3700/cm at around 3450/cm show the broad vibrational band of structural water molecules. These results reveal that deposited materials comprise structural water which designates the formation of hydrous CFP ($Co_xFe_{3-x}(PO_4)_2{\cdot}nH_2O$).

The N_2 isotherms (adsorption-desorption) of CFP-S2 are depicted in Fig. 2(C) and for other CFP-S1, CFP-S5 samples are provided in Figs. S2 (A and C). The isotherms of the samples are of the BET category with type-IV isotherm profiles having mesoporosity showing large adsorption energy [38]. The specific surface areas measured from the BET isotherms have the values of 25.63, 29.12, and 12.7 m^2/g for the samples CFP-S1, CFP-S2, and CFP-S5, accordingly. It is noted that the sample CFP-S2 has a higher surface area than the pristine cobalt phosphate (CFP-S1) and iron phosphate (CFP-S5). It underscores that metal composition leads to alteration in morphology and consequently

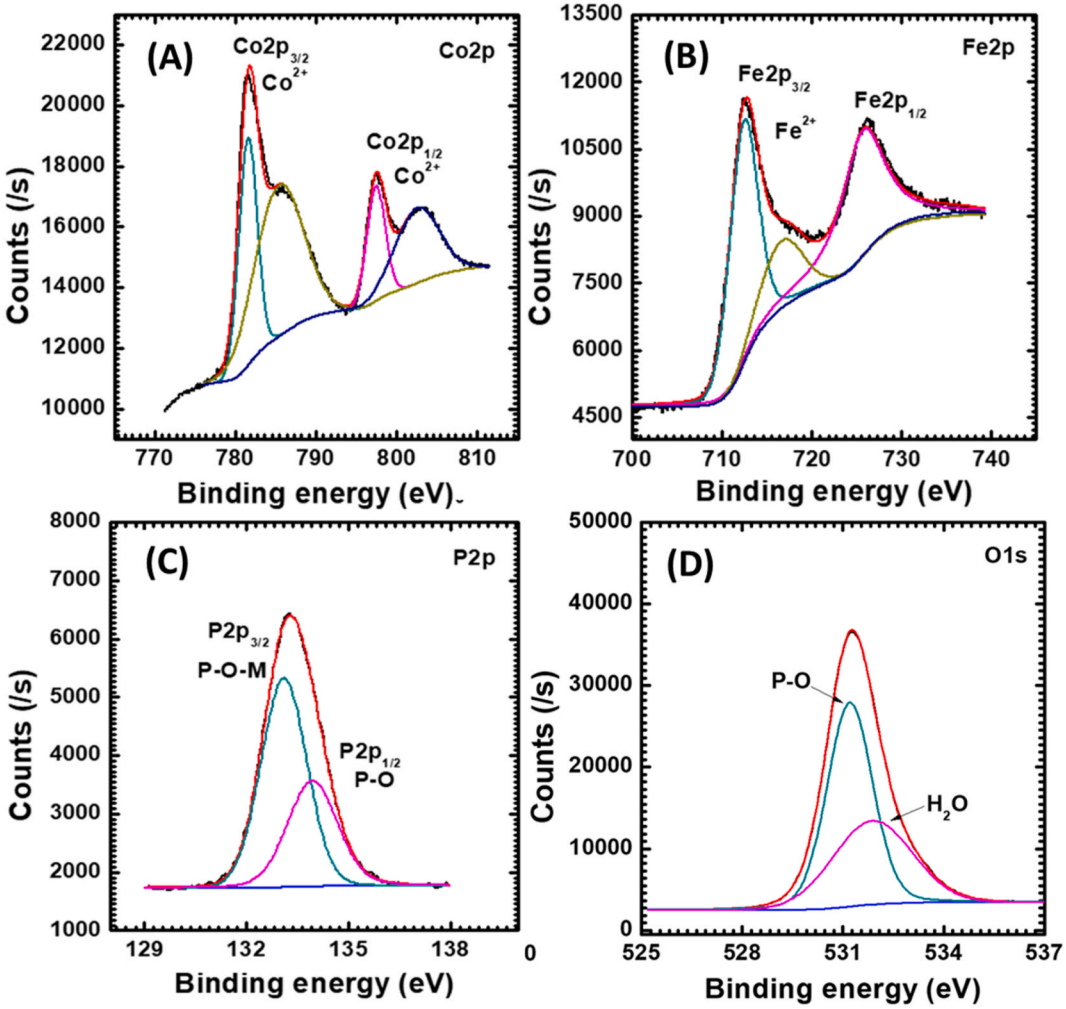

Fig. 3. High-resolution XPS spectra of **(A)** Co2p, **(B)** Fe2p, **(C)** P2p, and (**D**) O1s for CFP-S2 thin film electrocatalyst.

enhancement of surface area. The smaller surface area values for the CFP-S1 and CFP-S5 materials can be ascribed to the surface area's apparent dependence on irregular overgrowth into a particle size. The pore size distribution of the catalysts can be evaluated from the BJH method shown in the inset of Fig. 2(C), and Figs. S2(B and D). It demonstrates that the pore sizes range from 1 to 10 nm for the CFP series, confirming the mesoporous structure of the active materials. The material's large specific surface area and tiny pore size promote an interface area of electrolyte-electrode and offer a significant number of electroactive sites for the mass transfer and adsorption of –OH species, which may enhance the material's electrochemical water-splitting performance.

The electronic states and chemical bonding of elemental species in the present material were examined with XPS. The survey spectrum confirms that P, Fe, O, and Co elements are present in the CFP-S2 material (Fig. S3). The spectrum for each element can be resolved in their particular binding energy range. There are two major peaks in the maximum resolution of cobalt (Fig. 3(A)), at 781.76 and 797.43 eV along with two satellite peaks at 786.19 and 802.38 eV corresponding to $Co2p_{3/2}$ and $Co2p_{1/2}$, respectively. This confirms the Co^{2+} electronic state of the observed Co element [39]. Similarly, the prominent peaks located at 712.21 and 725.66 eV consist of $Fe2p_{3/2}$ and $Fe2p_{1/2}$ in the high-resolution spectrum of iron (Fig. 3(B)), corresponding to Fe^{2+} state [40,41]. Also, the phosphorous peak is deconvoluted into $P2p_{3/2}$ at 133.09 eV represents P–O-M bonding, and the peak at 133.9 eV which represents P–O bonding and consisting of P^{5+} oxidation state (Fig. 3(C)) [42–44]. In the spectrum of oxygen as presented in Fig. 3(D), the observed broad peak of oxygen is deconvoluted into two 531.23, and 532.83 eV, consisting of P–O bonds in phosphate and the surface adsorbed water molecules, respectively [45,46].

The morphology of CFP thin films was analyzed by FE-SEM. The surface topography of CFP-S2 thin film at 25 kX magnification is displayed in Fig. 4(A). Images at various magnifications for all thin film samples showed that the alteration in morphology of the materials with change in average particle sizes as the CFP-S1 to CFP-S5 composition varies (Fig. S4(A-O)). The spherical nanoparticles of ~110 nm average particle size are uniformly distributed and cover the surface of the substrate (Fig. 4(A)) in the CFP-S2 sample. The nanospheres are irregularly arranged over the surface forming a wide porous structure and altered average particle size influences specific surface area of CFP series samples. Furthermore, the EDS analysis associated with FE-SEM was utilized to support the study of chemical composition. The elemental mapping shown in Fig. 4(B) confirms the continuous distribution of Co, P, Fe, and O elements within the synthesized CFP-S2 sample. The CFP-S series electrodes were EDS characterized as given in Fig. S5 and the obtained atomic percentage (At %) ratios of cobalt to iron are 100:0, 75.52:24.48, 50.47:49.53, 23.26:76.74, and 0:100 for the CFP-S1, CFP-S2, CFP-S3, CFP-S4, and CFP-S5. The ratio of the phosphorous to oxygen was maintained around 20:80. Based on the EDS analysis, it is manifest that the observed nickel and cobalt molar proportions for CFP-S series samples are quite similar to the experimental compositions (Table S1). Moreover, to achieve thorough insights into the nanostructure of CFP-S2, the TEM analysis was carried out. Fig. 4(C-E) depicts the TEM images and selected area electron diffraction (SAED) pattern of CFP-S2 sample. The TEM image in Fig. 4(C) reveals spherical nanoparticles with a size of approximately 110 nm. It confirms that the size of nanoparticles observed by the FE-SEM and TEM images is consistent. The HR-TEM image presented in Fig. 4(D) exhibits no discernible fringe patterns which consist of disordered lattices. Also, the SAED pattern shown in Fig. 4(E) displays a dispersed halo devoid ring. No obvious lattice fringes and dispersed halo rings indicate the material is amorphous in nature. The TEM element mapping results of CFP-S2 are presented in Fig. 4(F), highlighting the presence of cobalt, iron, phosphorus, and oxygen with nearly similar At% to the EDS analysis. The findings from the TEM

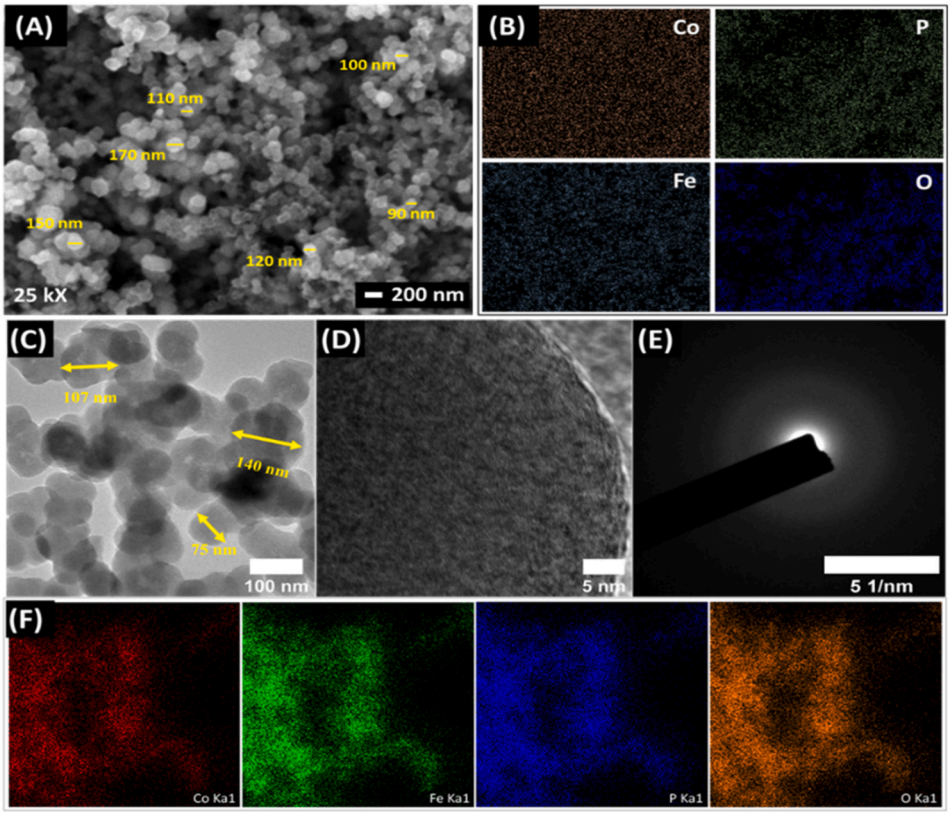

Fig. 4. Surface morphological and elemental study of CFP-S2 thin film: **(A)** FESEM image at 25 kX magnification, **(B)** EDS elemental mapping, **(C, D)** TEM and HR-TEM images, **(E)** SAED pattern, **(F)** TEM elemental mapping.

analysis align with the results obtained from XRD, FE-SEM and EDS, confirming the predominantly amorphous and nano-spherical particles of cobalt iron phosphate. The EDS results approve a variation in the Co: Fe molar ratio in CFP thin films, and optimal composition can provide improved electrochemical active sites owing to the synergy among them. CFP-S series electrodes may possess a large area of surface and hence a larger amount of electrochemical active sites for the water molecule adsorption and oxidation with such a nanospherical surface morphology and optimal cations composition.

3.3. Electrochemical catalytic performance analysis

As metals such as cobalt and iron can affect the electrocatalytic performance of the synthesized materials, the atomic ratios of cobalt and iron were adjusted to determine a suitable catalyst composition. Aiming to approve the hypothesis, an analysis of electrocatalytic oxygen and hydrogen evaluation was carried out. Electrochemical water splitting tests of CFP series material electrodes were performed in terms of OER and HER.

ECSA was calculated by the CV measurement, which is associated with the double-layer capacitance (C_{dl}). Fig. S6(A-E) shows the CV curves that formed using a small potential window (varying from 1.05 to 1.2 V vs. RHE) and several scan rates in the non-Faradic region. The plot of anodic charging current (i_c) vs scan rate is plotted using the following equation to determine C_{dl}:

$$i_c = vC_{dl} \quad (4)$$

Where v is the scan rate. The measured slopes of the plots are equal to C_{dl} as shown in Fig. 5(A). C_{dl} is found to be 5.05, 9.16, 7.55, 5.37, and 5.22 mF/cm^2 for CFP-S1, CFP-S2, CFP-S3, CFP-S4, and CFP-S5 catalysts, respectively. To determine the ECSA, the Cdl values are divided by the general specific capacitance (C_s) of the material's atomically flat planar real surface area (1 cm^2) under identical electrolyte conditions. Normally, C_s is 0.04 mF in an alkaline solution [47]. The evaluated ECSAs are 126.25, 229, 188.75, 134.25, and 130.5 cm^2 for CFP-S1, CFP-S2, CFP-S3, CFP-S4, and CFP-S5. The present comparison clarifies that the calculated highest ECSA is 229 cm^2 for the CFP-S2 electrode. By dividing the geometric region of the electrode that interacts with the electrolyte by the ECSA, the roughness factor (RF), or texture of the electrocatalytic interface was calculated. In the present study to measure electrochemical activity, 1 cm^2 area of the prepared thin films was used. Hence, RF are 126.25, 229, 188.75, 134.25, and 130.5 for CFP-S1, CFP-S2, CFP-S3, CFP-S4, and CFP-S5 electrodes, accordingly. Comparatively high RF demonstrates the availability of many electrocatalytic sites for electrolyte exposure. The results of the BET surface study are consistent with those from sample CFP-S2 and show exceptionally high ECSA and RF compared to the other catalysts.

The electrochemical OER was studied by the LSV recorded to the prepared materials at a scan rate of 1 mV/s. For CFP series electrodes, LSV curves are illustrated in Fig. 5(B). It has been found that all LSV polarization curves have a similar characteristic, and increasing potential is accompanied by a continual rise in current density. It is confirmed that the sample CFP-S2 is electrochemically most active and possesses a lower overpotential of 242 mV to achieve the 10 mA/cm^2 current density demonstrating outstanding performance for oxygen evolution. In distinction, other materials (CFP-S1, CFP-S3, CFP-S4, and CFP-S5)

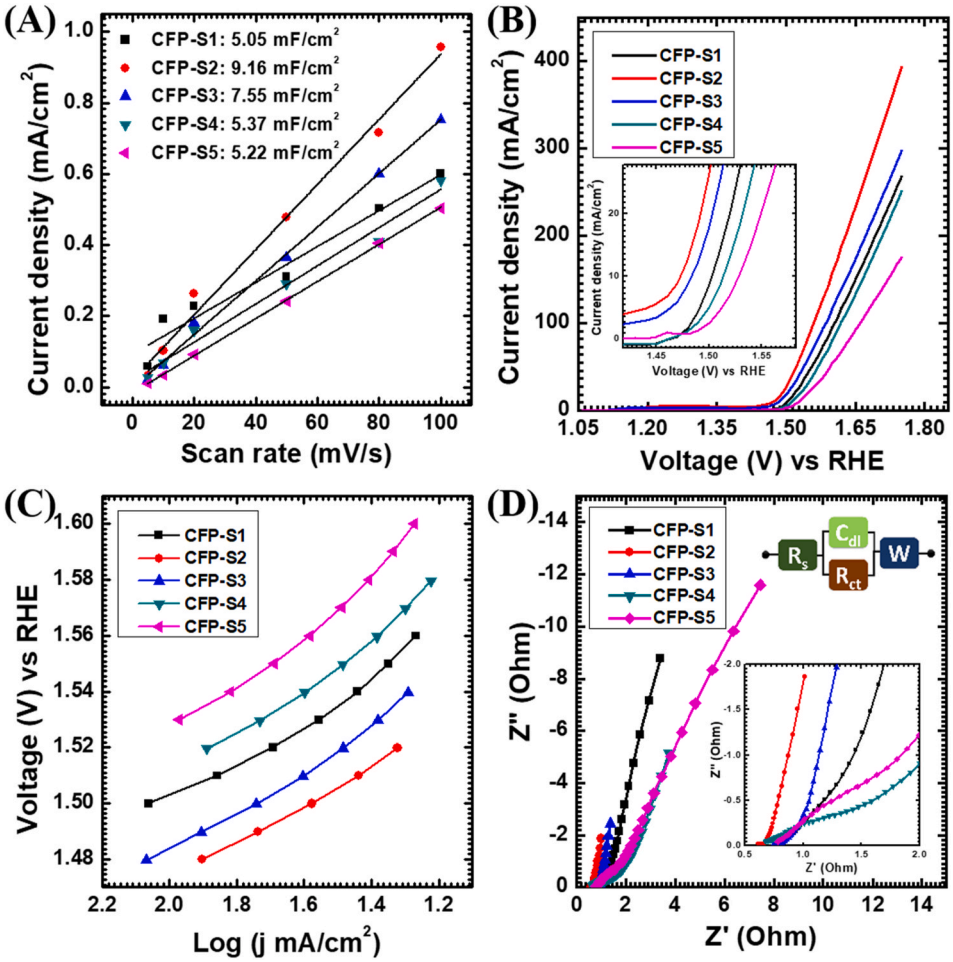

Fig. 5. Electrochemical analysis of CFP thin film materials: **(A)** plot of anodic currents vs scan rate, **(B)** OER analysis in terms of LSV, **(C)** Tafel slope, and **(D)** EIS.

demonstrated comparatively high overpotentials. O_2 molecule formed at the surface of the catalyst is only possible when a catalyst has a stronger OH^- ion attraction to sorb at the surface and creates an intermediate state. These reaction steps become rate-determining when the creation of these intermediate states happens more quickly. The Tafel slope, which was derived by plotting the applied overpotential against the logarithmic current density at the current density shoot-point as illustrated in Fig. 5(C), was used to evaluate the reaction rate kinetics. It reveals the 38.33 mV/dec Tafel slope for the catalyst CFP-S2, which is dramatically lesser than CFP-S1 (44.73 mV/dec), CFP-S3 (46.11 mV/dec), CFP-S4 (59.52 mV/dec), and CFP-S5 (69.73 mV/dec). It indicates that the CFP-S2 surface of the electrode exhibits highly effective kinetics of the reaction, and the OER reaction process is quicker, which is advantageous for O_2 production. According to the EIS plot (Fig. 5(D)), the CFP-S2 electrode has a significantly lower charge transfer resistance (R_{ct}). For the electrodes CFP-S1, CFP-S2, CFP-S3, CFP-S4, and CFP-S5, the fitted R_{ct} values are 0.89, 0.047, 0.43, 1.42, and 1.94 Ω, respectively. The EIS plot shows that there is a much smaller R_{ct} of the CFP-S2 electrode (Fig. 5(D)). As a result of the metal atoms' synergistic influence on the CFP-S series sample's low overpotential, it exhibits simple charge transfer.

The ability of an electrode material to function as an efficient catalyst for OER and HER must be determined by its catalytic stability. For the highest performed material (CFP-S2), the CA test at overpotential was carried out for 24 h as illustrated in Fig. S7. The material becomes more effectively catalytic during the catalysis process, and the electrode CFP-S2 performs better consequently. The material was first activated, causing the current density to initially increase and then stabilize for up to 24 h. The LSV plots of before and after 24 h of catalysis are displayed in Fig. S8, which reveals that overpotential drops from 242 to 237 mV and current density increases quickly at higher potential; concurrently, the Tafel slope also declines to 34.78 mV/dec after stability (Fig. S9). Following a stability test, the EIS was conducted, and it can be seen from the fitted equivalent circuit shown in the inset of Fig. S10 that R_{ct} falls from 0.047 to 0.034. Table S2 lists the electrochemical OER analysis before and after the CFP-S2 electrode was used for 24 h.

Further, to study HER, the polarization curves were recorded for CFP-S series electrodes in the potential window of 0.33 to -0.65 V vs RHE. All LSV polarization curves have a similar nature, and a steady increase in current density is observed. The measured overpotentials at -10 mA/cm^2 current density are 95.7, 67.9, 121.8, 177.4, and 220.9 mV for CFP-S1, CFP-S2, CFP-S3, CFP-S4, and CFP-S5 catalysts, respectively as shown in Fig. 6(A). It is observed that to deliver a current density of 10 mA/cm^2, the CFP-S2 electrode required the lowest overpotential. To assess faster HER, the rate-determining kinetics were evaluated by plotting the Tafel slope (Fig. 6(B)). The Tafel slope for CFP-S1, CFP-S2, CFP-S3, CFP-S4, and CFP-S5 catalysts are 36.47, 35.92, 38.23, 42.26, and 40.20 mV/dec, respectively. It reveals that the incorporation of iron up to a particular extent helps to decrease the reaction potential. Besides, the R_{ct} relevant to EIS spectra of CFP series electrodes were compared in Fig. 6(C). For the catalysts, CFP-S1, CFP-S2, CFP-S3, CFP-S4, and CFP-S5, the fitted R_{ct} values are 0.806, 0.589, 1.168, 2.354, and 4.273 Ω, respectively. As expected, the CFP-S2 exhibited a small interfacial charge-transfer resistance and a faster reaction rate. This corroborates that, low R_{ct} leads to the fast reaction kinetics, easy catalysis process, and low overpotential.

Another requirement for a top-notch electrocatalyst is stability. Chronoamperometry performed 24 h of overpotential catalytic stability testing on the best-performed catalyst electrode (CFP-S2). As shown in Fig. S11, the CFP-S2 catalyst became much more active and delivered enhanced current density after 24 h. Before and after the HER catalysis, the performances were compared by comparing LSV curves. It is observed that the overpotential decreased from 67.9 to 48.9 mV for the CFP-S2 electrode (Fig. S12). The plot of the Tafel slope (Fig. S13) reveals that the slope decreases to 32.56 mV/dec from 33.42 mV/dec signifying that the HER process remains faster after catalysis of 24 h. According to fitted EIS curves before and after the stability test, R_{ct} decreased from 0.589 to 0.492 Ω after 24 h of catalysis, which is expected given the increase in performance (Fig. S14). Table S2 summarizes the electrochemical HER analysis before and after the 24 h catalysis. It is concluded that the SILAR synthesized CFP thin film electrode shows enhanced performance. Moreover, the comparison between LSV curves of cobalt phosphate (CP), iron phosphate (FP), CFP, and SS for OER and HER is shown in Fig. 7(A–C). The synergistic interactions between the metal atoms are shown in the Fig. 7 to show how electrochemical performance is enhanced. The above evidence of SILAR synthesized CFP-S2 on SS substrates, including overpotential and Tafel slope is much superior to previous reports as shown in Fig. 7(B–D) [11,25,26,28,48–74].

An additional advantage is the simplicity of use when an electrolyzer uses a similar catalyst material on both electrodes (cathode for HER and anode for OER) for electrochemical water splitting. Consequently, the process can be made simpler by concurrently depositing both catalysts on the anodes and cathodes in integrated systems [73]. By preparing an alkaline electrolyte and the same catalyst material cathode and anode electrodes, overall water electrolysis was tested in 1 M KOH electrolyte as shown schematic representation in Fig. S15(A). Photographs of cells and electrodes during oxygen and hydrogen evolution are given in ESI as Fig. S15(B, B'). For the study of the robustness of the catalyst material, long-term water splitting stability (100 h) was conducted for the best-performing catalyst (CFP-S2). The effect of long long-duration water-splitting process on the electrochemical, structural, surface electronic states, and morphological properties of the catalyst material was also analyzed by conducting postmortem characterizations.

The LSV at a scan rate of 1 mV/s was conducted in the 0–2 V

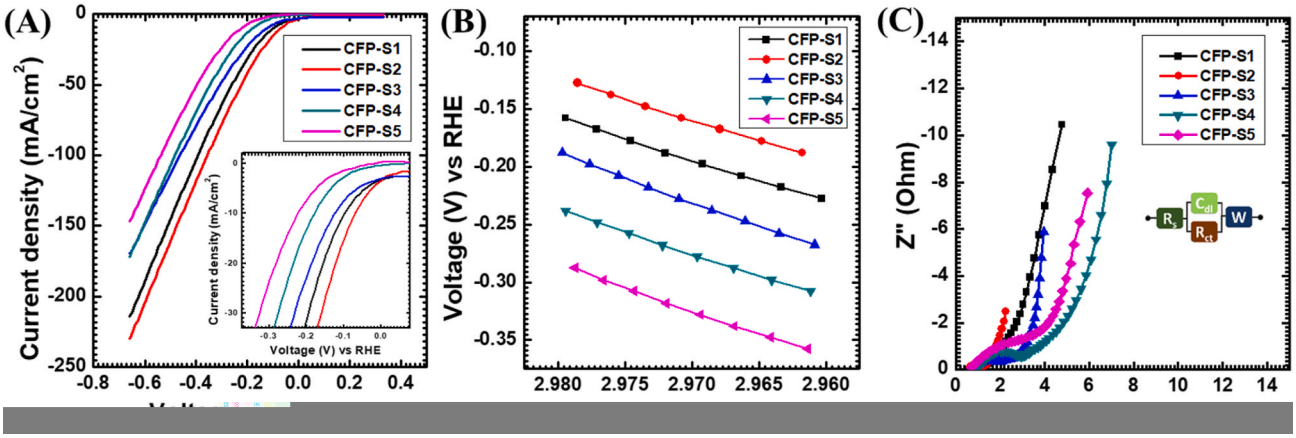

Fig. 6. Electrochemical analysis of CFP thin film materials: **(A)** HER analysis in terms of LSV, **(B)** Tafel slope, and **(C)** EIS.

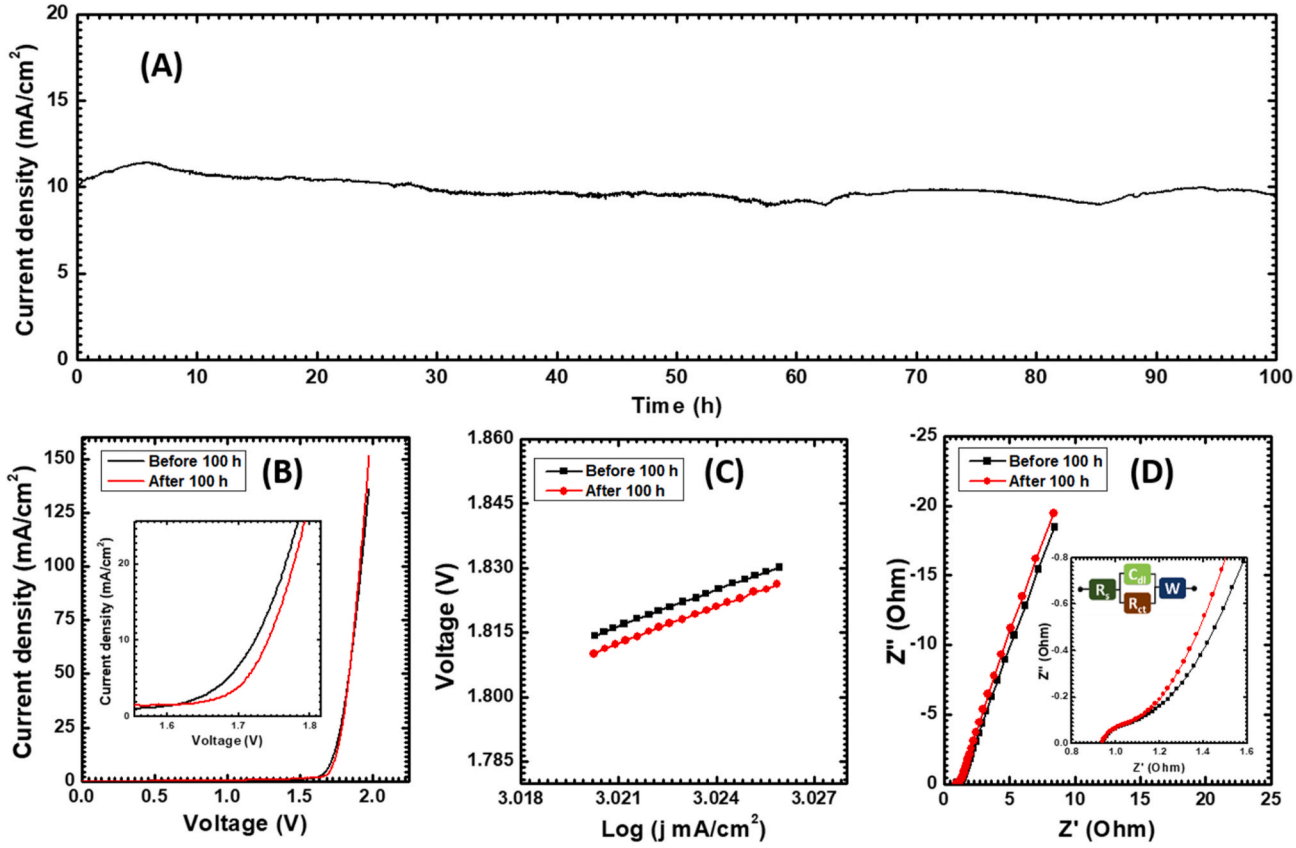

Fig. 8. Electrochemical overall water splitting stability **(A)** CA (I-t) plot, **(B)** LSV before and after 100 h catalysis, **(C)** Tafel plots, **(D)** EIS spectra recorded at OCP of the CFP-S2 catalyst.

separate peaks that form up the Co2p$_{3/2}$ peak are located at energies of 779.53 and 780.89 eV, respectively, and are linked to the existence of Co^{3+} and Co^{2+} ions. Two distinct peaks can be seen in the Co2p$_{1/2}$ peak, which correlates to the existence of Co^{3+} and Co^{2+} ions, respectively, at energies of 794.62 and 796.31 eV [37]. The Fe2p$_{3/2}$ peak is apparent at 710.73 eV in the XPS spectra of a Fe2p state, which is shown in Fig. S19 (C), and it is accompanied by a satellite peak at 717.86 eV [74]. In the spectra, the Fe2p$_{1/2}$ peak is seen at 723.92 eV, and a satellite peak is seen at 733.03 eV. The peaks Fe2p$_{3/2}$ contains two peaks associated with the Fe^{3+} and Fe^{2+} states having binding energies of 710.24 and 712.74 eV. Also, Peak Fe2p$_{1/2}$ is composed of 723.75 eV and 725.67 eV peaks correspond to states of Fe^{3+} and Fe^{2+}, individually. Existence of Fe^{3+} and Fe^{2+} electronic oxidation states together of Fe atoms and Co^{2+} and Co^{3+} electronic oxidation states of Co can be seen because of the oxidation of the catalyst material and partial transformation from Fe^{2+} to Fe^{3+} and Co^{2+} to Co^{3+} during 100 h continuous electrolysis. The phosphorous P2p shows a peak at 132.11 eV corresponding to the P2p$_{3/2}$ pentavalent state of phosphorus (Fig. S19(D)). After 100 h of catalysis, the partial conversion of phosphate into stable metal oxides demonstrates that there is depletion in the content of phosphorous. The O1s prominent peak is made up of three distinctive peaks as demonstrated in Fig. S19(E). The intense peak at 529.23 eV is accredited to M−O bonding and peaks at 530.73 eV, and 531.09 eV correspond to P–O bond and surface adsorbed water molecules, respectively [44]. As compared to O1s before stability, the M−O bond is increased tremendously which confirms the partial conversion into stable metal oxides.

3.5. Electrolyzer device demonstration

Research endeavors often aim to develop innovative and efficient technologies, products, or processes that can eventually be transformed into practical applications with real-world benefits. We have utilized a calibrated CFP-S2 electrocatalyst and quantified electrochemical overall water splitting from the same alkaline bath with volumetric measurement of evolved (O_2 and H_2) gases simultaneously, as revealed in schematic Fig. 9(A). The device contains a large glass container having electrolyte and electrode holder arrangement made by Teflon with constant power supply connections where the catalyst deposited electrodes were connected inverted. The inverted funnel and pipette were arranged on the top of the electrodes to collect evolved gases separately. The actual electrolyzer device is shown in the photograph in Fig. 9(B). Initially, the height of the electrolyte was adjusted to zero with the help of suction pumps. With the application of 1.72 V potential between two electrodes, the system delivers ~10 mA current and the gas bubbling was observed intensively (Fig. 9(C)). The experiment was conducted for a long duration and measured the volumes of the O_2 and H_2 gases that evolved in the form of displacement from the zero position. The measurements were performed at different time intervals (Fig. S20(A-G)) and plotted in the form of a bar diagram as shown in Fig. 9(D). The obtained ratios openly attest to the evolution of gases, with the amount of H_2 being approximately twice as large as the amount of O_2. This observation demonstrates the effective reactivity and selectivity of the catalysts in promoting the desired electrochemical reactions for water splitting.

As an overview, the SILAR-deposited CFP-S2 thin film electrodes deliver outstanding electrochemical performance. The as-synthesized binder-free CFP-S2 thin film electrode requires the smallest overpotentials for OER, HER, and water splitting. Moreover, the electrolyzer device using CFP-S2 electrodes demonstrates good performance. It is well known that; the SILAR is one of the best methods for the preparation of various materials at nanoscale having an amorphous nature. The presently synthesized CFP catalyst material has an amorphous nature. It

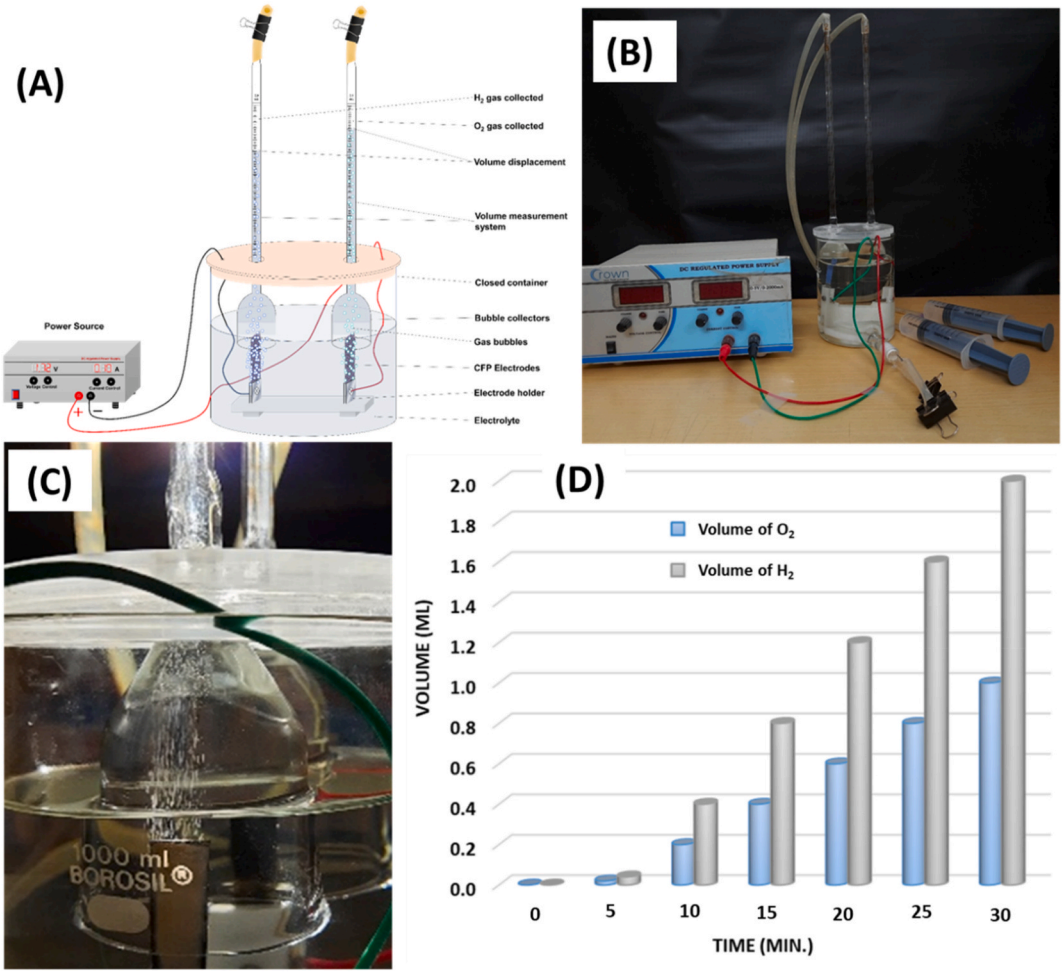

Fig. 9. **(A)** Schematic of the lab-made electrolyzer device for overall water splitting and gases collection with their volume measurements, Overall water splitting and volumetric measurement of gases: **(B)** Set-up of lab-made electrolyzer device for overall water splitting and volumetric measurement of gases evolved, **(C)** photograph during gases evolved from the electrode, **(D)** Graphical representation of volume change as a result of O_2 and H_2 gases evolved in experiment with respect to the time.

has nanospherical morphology along with improved surface area and mesoporous structure is more suitable for OH^- ion intercalation, adsorption, and making an intermediary state for the easy generation of O_2 molecules at the surface. The distinct combination of the metal cation elements (Co/Fe = 75.52/24.48) in CFP electrocatalyst is accredited with the electrochemical performance as it fosters the optimal environment for the absorption and oxidation of electrolyte ions. The conversion of electronic states and the stable compound leads to a stable current density during the long-term catalysis process, which proves the durability and robustness of the synthesized material.

4. Conclusions

The SILAR-synthesized CFP thin film electrocatalysts for the electrochemical water-splitting electrolyzer device were reported for the first time. The amorphous and mesoporous nanospherical morphology of the developed material facilitated the high electrochemically active surface area and large number of sites. By altering the cobalt/iron atomic ratio, the composition of CFP (Co:Fe) was optimized for OER and HER. The optimized CFP-S2 electrodes required the lowest overpotentials of 242 mV for OER, and 67.9 mV for HER, respectively to deliver 10 mA/cm^2 current density with outstanding stability for the period of 24 h. The water splitting was performed within a similar alkaline environment for the duration of 100 h by configuring an electrode system. The CFP-S2 electrode needs only 1.72 V to break the molecule of water into H_2 and O_2 gases with outstanding stability and material robustness. The lab-made device was operated using the as-synthesized CFP-S2 electrodes, which resulted in the evolution of approximately 0.06 ml/min of H_2 gas. The obtained ratios provide clear evidence of the evolution of gases, with the amount of H_2 being approximately twice as large as the amount of O_2. The present study proves that the effective and selective performance of SILAR-deposited CFP (CFP-S2) catalyst material facilitates the desired electrochemical reactions for water splitting.

Declaration of competing interest

The authors declare that they have no known competing financial interests or personal relationships that could have appeared to influence the work reported in this paper.

Acknowledgment

This research was supported by the Brain Pool program funded by the Ministry of Science and ICT through the National Research Foundation of Korea (2022H1D3A2A01093686). This work was supported by the National Research Foundation of Korea (NRF) grant funded by the Korea government (MSIT) (No. 2020R1A5A1019131).

Appendix A. Supplementary data

Supplementary data to this article can be found online at https://doi.org/10.1016/j.ijhydene.2024.02.259.

References

[1] Zou X, Zhang Y. Chem Soc Rev 2015;44:5148–80.
[2] Liu B, Zhao Y, Peng H, Zhang Z, Sit C, Yuen M, Zhang T, Lee C, Zhang W. Adv Mater 2017;29:1606521.
[3] Rand D, Dell R. Hydrogen energy: challenges and prospects. 2007.
[4] Sakamoto M, Izuhara D, Sotouchi H, Aoyagi F. Meet Abstr 2019;236:1703.
[5] Yoshida T, Kojima K. Electrochem Soc Interface 2015;24:45.
[6] Grätzel M. Nature 2001;414:338–44.
[7] Iaquaniello G, Giacobbe F, Morico B, Cosenza S, Farace A. Int J Hydrogen Energy 2008;33:6595–601.
[8] Lubitz W, Tumas W. Chem Rev 2007;107:3900–3.
[9] Bajdich M, García-Mota M, Vojvodic A, Nørskov J, Bell A. J Am Chem Soc 2013;135:13521–30.
[10] Haynes W. CRC handbook of chemistry and physics. 2014.
[11] Khalate S, Kadam S, Ma Y, Pujari S, Marje S, Katkar P, Lokhande A, Patil U. Electrochim Acta 2019;319:118–28.
[12] Cao L, Luo Q, Chen J, Wang L, Lin Y, Wang H, Liu X, Shen X, Zhang W, Liu W, Qi Z, Jiang Z, Yang J, Yao T. Nat Commun 2019;10:4849.
[13] Jiang R, Tung S, Tang Z, Li L, Ding L, Xi X, Liu Y, Zhang L, Zhang J. Energy Storage Mater 2018;12:260–76.
[14] Siracusano S, Dijk N, Payne-Johnson E, Baglio V, Aricò A. Appl Catal B 2015;164:488–95.
[15] Cherevko S, Geiger S, Kasian O, Kulyk N, Grote J, Savan A, Shrestha B, Merzlikin S, Breitbach B, Ludwig A, Mayrhofer K. Catal Today 2016;262:170–80.
[16] Yuan C, Jiang Y, Zhao Z, Zhao S, Zhou X, Cheang T, Xu A. ACS Sustainable Chem Eng 2018;6:11529–35.
[17] Ahn S, Tan H, Haensch M, Liu Y, Benderskya L, Moffat T. Energy Environ Sci 2015;8:3557–62.
[18] Fan G, Li F, Evans D, Duan X. Chem Soc Rev 2014;43:7040–66.
[19] Li L, Wang P, Shao Q, Huang X. Chem Soc Rev 2020;49:3072–106.
[20] Yan Y, Yu Xia B, Zhao B, Wang X. J Mater Chem A 2016;4:17587–603.
[21] Tang C, Zhang R, Lu W, Wang Z, Liu D, Hao S, Du G, Asiri A, Sun X. Angew Chem Int Ed 2016;55:1–6.
[22] Xie L, Zhang R, Cui L, Liu D, Hao S, Ma Y, Du G, Asiri A, Sun X. Angew Chem Int Ed 2016;56:1064–8.
[23] Wang J, Cui W, Liu Q, Xing Z, Asiri A, Sun X. Adv Mater 2016;28:215–30.
[24] Khalate S, Kadam S, Ma Y, Kulkarni S, Parale V, Patil U. J Colloid Interface Sci 2022;613:720–32.
[25] Zhou Y, Zeng H. Small 2018;14:1704403.
[26] Wang Z, Liu M, Du J, Lin Y, Wei S, Lu X, Zhang J. Electrochim Acta 2018;264:244–50.
[27] Zhang J, Tan X, Wang W, Cao L, Dong B. Sustain Energy Fuels 2020;4:4704–12.
[28] Yin D, Jin Z, Liu M, Gao T, Yuan H, Xiao D. Electrochim Acta 2018;260:420–9.
[29] Zou Y, Liu Z, Liu R, Liu D, Dong C, Wang Y, Wang S. J Power Sources 2019;427:215–22.
[30] Han H, Choi H, Mhin S, Hong Y, Kim K, Kwon J, Ali G, Chung K, Je M, Umh H, Lim D, Davey K, Qiao S, Paik U, Song T. Energy Environ Sci 2019;12:2443–54.
[31] Jiang Z, Lu W, Li Z, Ho K, Li X, Jiao X, Chen D. J Mater Chem A 2014;2:8603–6.
[32] Kale R, Lokhande C. Mater Res Bull 2004;39:1829–39.
[33] Pathan H, Lokhande C. Bull Mater Sci 2004;27:85–111.
[34] Guo T, Li L, Wang Z. Adv Energy Mater 2022;12:2200827.
[35] Zhang D, Soo J, Tan H, Jagadish C, Catchpole K, Karutur S. Adv. Energy Sustainability Res. 2021;2:2000071.
[36] Murugesan C, Lochab S, Senthilkumar B, Barpanda P. ChemCatChem 2018;10:1122–7.
[37] Li H, Yu M, Lu X, Liu P, Liang Y, Xiao J, Tong Y, Yang G. ACS Appl Mater Interfaces 2014;6:745–9.
[38] Condon J. Surface area and porosity determinations by physisorption: measurement, classical theories and quantum theory. 2019.
[39] Li Y, Wang Z, Hu J, Li S, Du Y, Han X, Xu P. Adv Funct Mater 2020;30:1910498.
[40] Roy N, Sohn Y, Leung K, Pradhan D. J Phys Chem C 2014;118:29499–506.
[41] Zhang Q, Li T, Liang J, Wang N, Kong X, Wang J, Qian H, Zhou Y, Liu F, Wei C, Zhao Y, Zhang X. J Mater Chem A 2018;6:7509–16.
[42] Jiang N, You B, Sheng M, Sun Y. ChemCatChem 2016;8:106–12.
[43] Gresch R, Muller-Warmuth W. J Non-Cryst Solids 1979;34:127–36.
[44] Li B, Shi Y, Huang K, Zhao M, Qiu J, Xue H, Pang H. Small 2018;14:1703811.
[45] Katkar P, Marje S, Pujari S, Khalate S, Lokhande A, Patil U. ACS Sustainable Chem Eng 2019;7:11205–18.
[46] Dan H, Tao K, Zhou Q, Gong Y, Lin J. ACS Appl Mater Interfaces 2018;10:31340–54.
[47] McCrory C, Jung S, Peters J, Jaramillo T. J Am Chem Soc 2013;135:16977–87.
[48] Khalate S, Kadam S, Ma Y, Pujari S, Patil U. J Alloys Compd 2021;885:160914.
[49] Li C, Mei X, Lam F, Hu X. ACS Appl Energy Mater 2018;1:6764–8.
[50] Bhanja P, Kim Y, Kani K, Paul B, Debnath T, Lin J, Bhaumik A, Yamauchi Y. J Chem Eng 2020;396:125245.
[51] Wang D, Xu Y, Sun W, Guo X, Yang L, Wang F, Yang Z. Electrochim Acta 2020;337:135827.
[52] Liu L, Zhang D, Duan D, Li Y, Yuan Q, Chen L, Liu S. J Electroanal Chem 2020;862:114031.
[53] Liu M, Lin Y, Wang K, Chen S, Wang F, Zhou T. Chin J Catal 2020;41:1654–62.
[54] Kim D, Kang J, Yan B, Seong K, Piao Y. ACS Sustainable Chem Eng 2020;8:2843–53.
[55] Li J, Zhou Q, Zhong C, Li S, Shen Z, Pu J, Liu J, Zhou Y, Zhang H, Ma H. ACS Catal 2019;9:3878. 388.
[56] Liu M, Qu Z, Yin D, Chen X, Zhang Y, Guo Y, Xiao D. Chemelectrochem 2018;5:36–43.
[57] Yue Q, Gao T, Wu Y, Yuan H, Xiao D. Electrochim Acta 2020;362:137123.
[58] Wu L, Shi L, Zhou S, Zhao J, Miao X, Guo J. Energy Technol 2018;6:2350–7.
[59] Babar P, Lokhande A, Shim H, Gang M, Pawar B, Pawar S, Kim J. J Colloid Interface Sci 2019;534:350–6.
[60] Yang Y, Fei H, Ruan G, Tour J. Adv Mater 2015;27:3175–80.
[61] Qian L, Miao Y. Polyhedron 2019;160:213–8.
[62] Babar P, Lokhande A, Jo E, Pawar B, Gang M, Pawar S, Kim J. J Ind Eng Chem 2019;70:116–23.
[63] Liang Q, Jin H, Wang Z, Xiong Y, Yuan S, Zeng X, He D, Mu S. Nano Energy 2019;57:746–52.
[64] Menezes P, Panda C, Walter C, Schwarze M, Driess M. Adv Funct Mater 2019;29:1808632.
[65] Menezes P, Indra A, Zaharieva I, Walter C, Loos S, Hoffmann S, Schlögl R, Dau H, Driess M. Energy Environ Sci 2019;12:988–99.
[66] Sial M, Lin H, Wang X. Nanoscale 2018;10:2975–12980.
[67] Qi J, Chen i, Zhang W, Cao R. Chin J Catal 2022;43:955–1962.
[68] haikh J, Rittiruam M, Saelee T, Márquez V, Shaikh N, Santos J, Kanjanaboos P, Nazeeruddin M, Praserthdam S, Praserthdam P. Mater Today Chem 2022;26:101267.
[69] Liu Y, Zhang S, Jiao C, Chen H, Wang G, Wu W, Zhuo Z, Mao J. Adv Sci 2023;10:2206107.
[70] Zhao R, Ni B, Wu L, Sun P, Chen T. Colloids Surf A Physicochem Eng Asp 2022;635:128118.
[71] Roy O, Jana A, Pratihar B, Saha D, De S. J Colloid Interface Sci 2022;610:592–600.
[72] Gajraj V, Devi P, Kumar R, Sundriyal N, Reddy M, Mariappan C. Int J Hydrogen Energy 2023;47:17868–81.
[73] Menezes P, Panda C, Loos S, Bunschei-Bruns F, Walter C, Schwarze M, Deng X, Dau H, Driess M. Energy Environ Sci 2018;11:1287–98.
[74] Kadam S, Phan G, Pham D, Patil R, Lai C, Chen Y, Liouc Y, Ma Y. Nanoscale Adv 2021;3:5581–8.